Role of Oxygen on the Precipitation and Deformation Behavior of an Aged β Ti-15Mo Alloy

Kathleen Chou, Emmanuelle A. Marquis*

Department of Materials Science and Engineering, University of Michigan, Ann Arbor, MI 48109 USA;

*Corresponding Author

Kathleen Chou
Dow Building
2300 Hayward St.
Ann Arbor, MI 48109
kachou@umich.edu
Phone: 248-925-7880

ORCID: 0000-0003-1974-4766

Emmanuelle A. Marquis (Corresponding Author) Dow Building 2300 Hayward St. Ann Arbor, MI 48109 emarq@umich.edu

Phone: 734-764-8717

ORCID: 0000-0002-6476-2835

Role of Oxygen on the Precipitation and Deformation Behavior of an Aged β Ti-15Mo Alloy

Kathleen Chou^a, Emmanuelle A. Marquis^{a*}

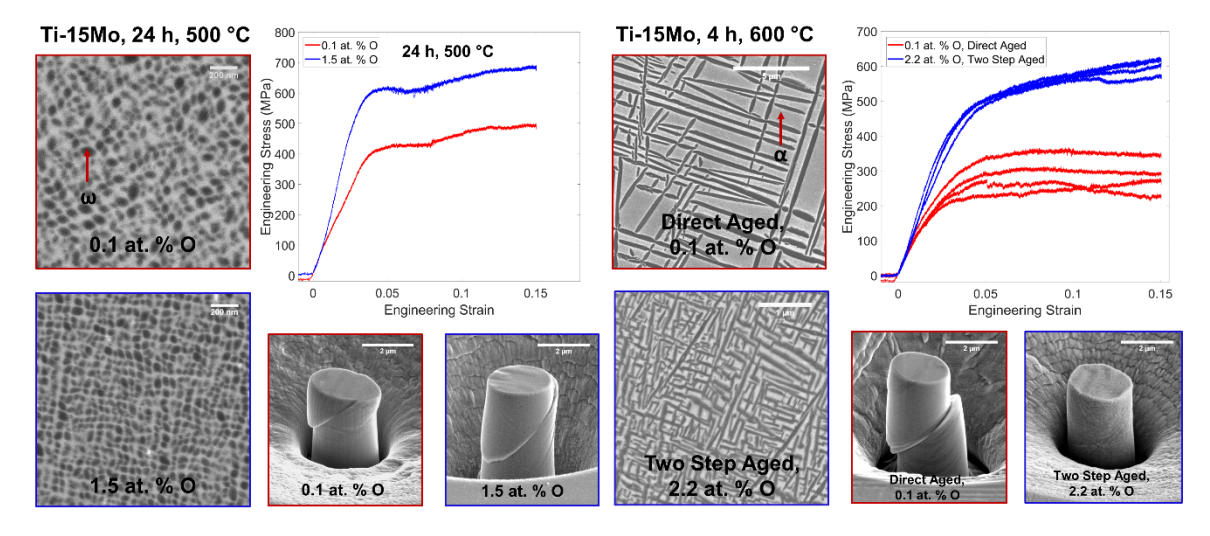
^a Department of Materials Science and Engineering, University of Michigan, Ann Arbor, MI 48109 USA

*Corresponding Author

Highlights

- Oxygen slows the growth of ω and changes ω precipitates to cuboidal shapes
- Oxygen partitioning to ω increases yield strength of compressed micropillars
- Oxygen-induced α refinement enables improved precipitation strengthening

Graphical Abstract



Abstract

The mechanical behavior of aged metastable β titanium alloys is directly influenced by the formation and stability of metastable ω and stable α phases during thermomechanical processing. Interstitial oxygen, which is known to cause embrittlement in Ti alloys, affects metastable and stable phase stability in these alloys that and also impacts their structural properties. The present study investigated the role of interstitial oxygen on ω and α precipitation in an aged metastable β Ti-15Mo alloy and the subsequent effect of these microstructural changes on the alloy's compressive mechanical properties. High oxygen levels reduced the ω growth rate and induced a

shape change for ω precipitates with oxygen partitioning to ω precipitates during ageing. Oxygen-containing specimens displayed higher compressive yield strengths than in oxygen-free specimens during micropillar compression testing. However, in both cases, ω precipitates were ultimately sheared leading to slip band formation and plastic flow localization. Elevated oxygen also refined the α precipitate distribution whether α nucleation happened homogeneously or heterogeneously. The finer α precipitates with oxygen led to increased compressive yield strength during micropillar compression compared to specimens without oxygen. Oxygen plays a key role in the evolution of ω and α precipitate distributions and associated mechanical properties, which is another example of how oxygen can may be a useful alloying element in β titanium alloys.

Keywords

Metals and alloys, Phase transitions, Precipitation, Microstructure, Mechanical properties, Titanium

1. Introduction

Metastable β titanium alloys have been the subject of continued scientific investigation and development due to their rich variety of microstructures and wide range of attainable mechanical properties depending on alloy chemistry and processing [1]. This range of properties allows their use in many applications including aerospace and biomedical components [2–4]. In β Ti alloys, the body centered cubic (bcc) β phase is stabilized to room temperatures by the addition of β -stabilizing elements such as Mo, V, and Nb, and a metastable β phase matrix is typically obtained after solution treatment and quenching. Depending on thermomechanical treatment, the metastable β state can also result in the formation of intermediate metastable phases such as α ' (hcp) and α " (orthorhombic) martensites [1], ω (hexagonal or trigonal) phase [5], and recently reported nanoscale phases [6–9] prior to stable α precipitation [1]. The formation and stability of metastable phases in β Ti alloys have been extensively investigated because of the link between these phases and desirable mechanical properties such as superlow elastic modulus, ultrahigh strength, and superelastic behavior [10–12].

Oxygen is another important element for β Ti alloys due to its unique effects on metastable and stable phase stability. In general, oxygen is highly soluble in α and β Ti phases [13], and significant ingress and dissolution of oxygen occurs during elevated temperature oxidation exposures for Ti and Ti alloys [14,15]. High levels of dissolved oxygen are known to embrittle α and β Ti phases, leading to increased hardness but reduced ductility [16]. While it has been well reported that O causes solid solution hardening and ductility reduction in α-Ti alloys [17], the ductility of selected β Ti alloys is not jeopardized by high oxygen levels in the range of 2.5-3.0 at. % (0.6 wt. %) [10,18], enabling the use of dilute oxygen levels in tailoring alloy microstructure and properties. However, rRecent investigations have shown that oxygen also enables significant changes in metastable phase stability for β Ti alloys, which impacts microstructural evolution and mechanical behavior. These changes include the suppression of large-scale martensite formation during quenching of Ti-Nb alloys that allows formation of nanoscale products such as nanodomains [19] and O' [8,20] leading to properties such as shape memory behavior [12], superelasticity [21,22] and unique thermal expansion behavior [23]. Elevated oxygen also affects the evolution of the metastable ω phase, which subsequently impacts mechanical behavior. ω formation is known to cause severe embrittlement in aged β Ti alloys [24–26], but ω has gathered renewed interest due to its role in changing the deformation mechanisms from transformationinduced plasticity and twinning-induced plasticity deformation mechanisms to dislocation slip [27,28], contributing on to strong and ductile β Ti alloys after short ageing treatments [29,30], and actinginfluence as a heterogeneous nucleation agent for stable α precipitation [31–34]. Elevated O levels have been reported to stabilize the ω phase and oxygen partitions to ω precipitates during ageing [35,36]. Furthermore, microstructures with O partitioning to large ω precipitates showed suppression of slip localization resulting in improved duetility and work hardening during micropillar compression of Ti-Nb alloys, which addresses known embrittlement challenges with isothermal ω formation without oxygen [37]. High oxygen levels also affect the precipitation kinetics of the stable α phase. Elevated O concentrations have been demonstrated to induce α phase refinement in an aged metastable β Ti-15-333 alloy, leading to increased compressive strengths and improved precipitation strengthening [38].

Ti-Mo alloys are an important subset of β titanium alloys due to the frequent use of Mo in commercial alloy compositions. Mo is a common addition to β Ti alloys due to its strong stabilization of the β phase resulting in cost-effective master alloys and low tendency for

solidification segregation [2]. When considering isomorphous β phase stabilizing elements Mo, Nb, Ta, V, and W, Mo has the lowest critical concentration to retain 100% of the β phase after quenching to room temperature [1], which enables a metastable β phase matrix with lower solute levels leading to lower overall alloy density that is important for weight-sensitive aerospace components. Although other β-stabilizing elements such as Cr and Fe have a lower critical concentration to retain 100% of the β phase upon quenching, these elements exhibit limited solid solubility in Ti, and a eutectoid reaction results in the formation of intermetallic compounds [1]. Fe and Cr also promote a wider mushy zone upon solidification of alloy ingots leading to issues such as greater constitutional undercooling, coring, and gross segregation that require more control during ingot melting [2]. The absence of intermetallic phases for Ti systems alloyed with isomorphous β phase stabilizing elements allows for a simpler system to understand O effects on microstructural evolution in β Ti. In the Ti-Mo system, oxygen can also affect precipitation kinetics and metastable phase stability. As-quenched microstructures of Ti-7.5Mo wt. % without O have shown martensite formation [39]. However, formation of the α phase in addition to martensite was reported for these alloys with high oxygen levels up to 0.5 wt. % O due to αstabilization with oxygen [39]. In a more solute-rich Ti-15Mo wt. % alloy, athermal ω phase formation was suppressed upon quenching with O levels up to 0.5 wt. %, and the deformation mechanism transitioned from twinning to dislocation slip in the presence of oxygen [40]. Oxygen played an important role in the formation of nanoscale phases reported for Ti-Nb based compositions [19,22]. However, in Ti-Mo alloys, the nanoscale O' phase was identified despite interstitial oxygen being intentionally removed [41]. Although these studies explored the influence of oxygen in Ti-Mo based compositions, extensive investigations have not been conducted for oxygen in relation to other metastable phases such as ω and the impact of microstructural changes with oxygen on mechanical properties. Yet, understanding the effects of interstitial oxygen on the microstructures and properties of Ti-Mo based alloys is an important area of investigation due to the frequent use of Mo in commercial β Ti alloy compositions and the low allowable oxygen levels in industrial alloy specifications due to embrittlement concerns.

In this study, Therefore, this study focuses on evaluating aged Ti-15Mo with varying oxygen content was evaluated to understand differences in ω and α precipitation kinetics and their impacts on mechanical behavior using micropillar compression. Heat treatments were selected to promote ω nucleation and growth with oxygen partitioning to ω while preventing α

phase formation. Higher temperature ageing was also conducted to induce α formation and understand oxygen's influence on α 's size and precipitation rate. Micropillar compression testing of ω containing microstructures with varying oxygen contents showed that ω with partitioned oxygen resulted in higher compressive yield strength and finer slip lines indicating less plastic flow localization than those without oxygen. Furthermore, the refinement of α precipitates with high oxygen after higher temperature ageing resulted in increased average compressive yield strengths compared to minimal oxygen specimens. While bulk tensile testing is needed to test any effect on ductility. These these results provide evidence of oxygen's beneficial effects on phase formation and the ensuing mechanical properties strength. The results may provide avenues to mitigate the conventionally accepted detrimental effects of interstitial oxygen in commercially relevant alloys and may enable future alloy design and processing methods specifically utilizing oxygen as an alloying element in β Ti alloys.

2. Materials and methods

Commercial alloy Ti-15Mo wt. % (Ti-8Mo at. %) with nominally less than 0.1 wt. % O was provided by ATI. Specimens were sectioned using a slow speed diamond saw, encapsulated in quartz tubes with Ar gas, solution treated homogenized by heat treating at 1000 °C for 24 h, and quenched by breaking the tube in water. A subset of solution treated samples was oxidized in a 1 standard cubic centimeter per minute (SCCM) $O_2/4$ SCCM Ar (20% O_2) environment at 900 °C for 5 hours. Oxygen concentration profiles in the β matrix after oxidation were measured on polished cross-sections using wavelength dispersive spectroscopy (WDS) in a Cameca SX100 electron microprobe as reported in [36,38]. Measurements of the O K α , Ti K α , and Mo L α X-rays were made using a focused electron beam with a beam current of 40 nA and accelerating potential of 15 keV. Calibration standards were synthetic MgO (O K α), Ti metal (Ti K α), and Mo metal (Mo L α); Additional details on the analysis of WDS data are located in Supplemental Supplementary Material.

As-solution treated samples and oxidized samples were subsequently encapsulated in quartz tubes with Ar gas and isothermally aged using the following conditions: 450 °C for 2 and 24 h, 500 °C for 24 h, and 600 °C for 4 h. Specimens were inserted into a preheated furnace such that the sample heating rate was > 5 °C/s. Complete dissolution of ω has been observed at 560 °C

in Ti-15Mo [42]. Therefore, ageing treatments for ω formation were conducted at 450 and 500 °C to promote fast ω precipitation and elemental partitioning while maintaining slower α precipitation kinetics. Ageing at 600 °C was also performed to induce direct α precipitation. Finally, a two_step ageing treatment was conducted with the first step at 450 °C for 2 h, followed by a second step at 600 °C for 4 h to investigate the effect of ω -assisted α precipitation with elevated oxygen content. Processing diagrams that give a visual description of the specific ageing treatments and parameters studied here are shownprovided in Supplementary Material.

Aged specimens were cross-sectioned using a slow speed diamond saw, mounted in epoxy, then ground using 320-1200 grit SiC papers and polished using 0.03 µm colloidal silica suspension. Scanning electron microscopy (SEM) imaging and focused ion beam (FIB) preparation of transmission electron microscopy (TEM) foils and needle-shaped atom probe tomography (APT) specimens were performed using a Thermo Fisher Scientific FEI Helios 650 Nanolab with a Ga⁺ ion FIB. TEM images and selected area electron diffraction (SAED) patterns were obtained using a Thermo Fisher Scientific Talos F200X G2 microscope operated at 200 kV. APT data collection was performed with a Cameca local electrode atom probe (LEAP) 5000 XR operated in laser mode. APT data was collected using a specimen temperature of 30 K, a detection rate of 0.005 atoms per pulse, laser pulse energy of 25 pJ, and pulse repetition rate of 200 kHz. Data reconstruction, background subtraction, peak deconvolution, and compositional analysis were performed using the AP Suite software package 6.1.

Due to the compositionally graded nature of specimens created after the oxidation exposure, micropillar compression testing was used to evaluate the compressive mechanical properties of local microstructural regions with varying oxygen content (corresponding to oxygen concentration profiles measured using WDS). A specific grain for pillar fabrication was selected in each specimen to be close to the (100)_β out of plane orientation after characterization using electron backscattered diffraction (EBSD) (Supplemental Supplementary Material). Single crystal micropillars with a 2 μm diameter were fabricated in the selected grain using FIB in a Thermo Fisher Scientific FEI Helios 650 Nanolab. Pillars were fabricated with an automated script with coarse annular milling at 30 kV, 9 nA and fine milling at 30 kV, 0.79 nA. Milled micropillars had a diameter-to-height aspect ratio of approximately 1 to 2.5 to avoid a triaxial stress state for low aspect ratios and pillar buckling at high aspect ratios [43]. Four Mmicropillars per condition were tested in compression in a Hysitron TI 950 Triboindenter with a flat punch indenter (60° cone

angle, 10 µm diameter flat end) in displacement-controlled mode with a strain rate of ~ 0.0005 s⁻¹. Tests were manually stopped at a predetermined displacement amount to characterize compressed pillars at specific strain levels. Compressive engineering stress-strain curves were calculated from collected load versus displacement data. The engineering stress was calculated as $\sigma = F/A_0$ where F is the measured force and A_0 is the cross-sectional area at the top of the pillar, and the engineering strain was calculated as $\varepsilon = \Delta L/L_0$ where ΔL is the pillar displacement and L_0 is the initial pillar height [44]. After compression, the morphology of deformed pillars was observed using SEM and TEM. Cross-sections and TEM foils of deformed micropillars were prepared using a cross-sectional FIB liftout technique similar to Refs. [45].

3. Results

3.1. Solution treated and oxidized Ti-15Mo prior to ageing

Solution treated and quenched Ti-15Mo contained a single β phase matrix with grain sizes greater than 500 µm. Following the oxidation exposure at 900 °C for 5 h, a thick, porous oxide scale without strong adherence to the base metal formed on specimen surfaces, and oxide spallation was frequently observed during specimen handling and sectioning. Specific oxide growth mechanisms and oxide morphologies are not the focus of this work. Precipitation of α laths about 50 μm in length was observed in the subsurface metal just below the oxide/metal interface of crosssectioned specimens (Figure 1a). Given oxygen's role as a potent α stabilizing element in Ti alloys, the formation of α laths in the outermost subsurface metal region during oxidation is consistent with oxygen dissolution in the β Ti matrix that stabilizes α and promotes its precipitation [13]. α formation is also accompanied by Mo rejection and partitioning from α to the β matrix, which is consistent with Mo as a β -stabilizer in Ti alloys [46]. Below the α lath + β matrix region, the single-phase β matrix contained interstitial oxygen that diffused in a concentration gradient during the oxidation exposure. This oxygen concentration profile was measured in the single-phase β matrix using WDS starting from the interface of the α lath + β matrix region near the sample's edges and moving towards the center of the cross-sectioned specimens (yellow arrow in Figure 1a). The average of four measured profiles (Figure 1b) illustrated that oxygen diffused to a depth of ~1 mm in the β matrix during oxidation, which is a similar diffusion depth reported for Ti-20Nb (at. %) after the same oxidation exposure [36]. This depth agrees with mean diffusion lengths estimated using reported oxygen diffusion parameters in the range of 54x*10⁻¹²⁴ to 15x*10⁻¹¹² m²/s at 900 °C in β Ti [47]. The maximum oxygen concentration of approximately 2.6 at. % O (0.8 wt. % O) was located at the interface between the α lath / β matrix regions. WDS measurements did not show changes for Mo concentration as a function of distance in the single-phase β matrix.

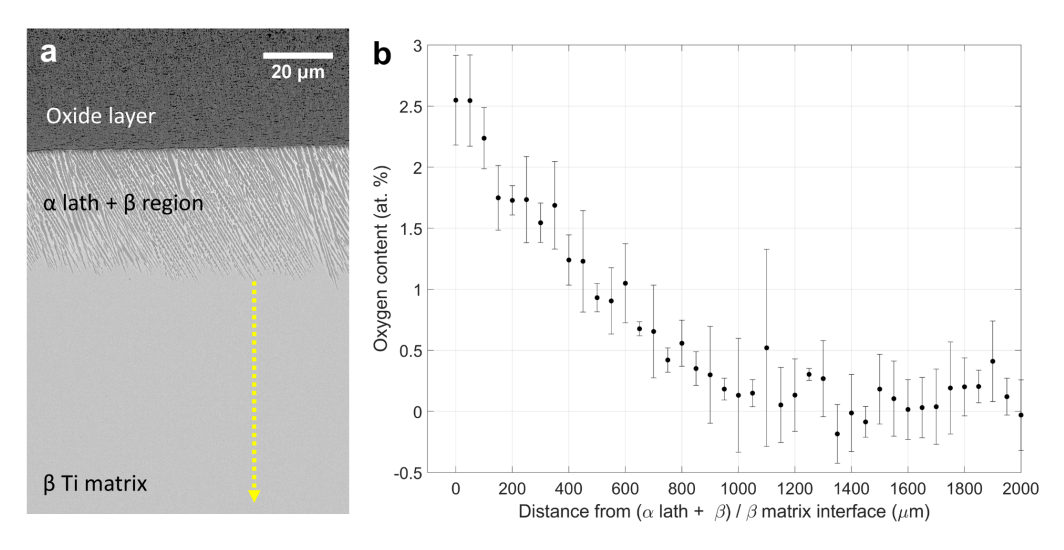


Figure 1. (a) SEM-BSE image of cross-section for oxidized Ti-15Mo showing porous oxide scale and α lath formation after oxidation exposure at 900 °C for 5 h. Yellow arrow indicates starting location and direction of WDS line traces. (b) Average and standard deviation of four WDS line traces measuring oxygen concentration beginning from the (α lath + β) / β matrix interface and traversing across the cross-section of oxidized Ti-15Mo.

3.2. ω precipitation and deformation in Ti-15Mo with varying oxygen content

As-solution treated specimens and oxidized specimens were subsequently aged to understand ω precipitation with varying oxygen levels. Specimens that were solution treated and aged with minimal oxygen content are hereafter referred to as *directly aged (DA)*, and specimens that were solution treated, oxidized, and then aged with the created oxygen diffusion gradient are hereafter referred to as *oxidized and aged (OXA)*. The microstructure characterized at specific distances from the α lath / β matrix interface towards the center of the sample in OXA oxidized and aged specimens corresponded to specific oxygen contents as measured by WDS (**Figure 1b**).

Directly agedA and OXA-oxidized and aged specimens aged at 450 °C for 2 h resulted in dense ~10 nm metastable ω precipitates observed in backscattered SEM (SEM-BSE) images

(Figure 2a-b). As expected from prior studies [48], elemental partitioning of Mo to the β matrix occurred as demonstrated by compositional contrast in SEM-BSE images. After 24 h of ageing at 450 °C, ω precipitates grew to ~20-30 nm in size. The ω particles in oxygen-free DA directly aged specimens exhibited ellipsoidal shapes, which is consistent with prior ω studies for the low misfit Ti-Mo system [48]. SEM-BSE images showed higher number densities of finer ω precipitates in the presence of oxygen compared to specimens without oxygen (Figure 2c-d). The OXA-oxidized and aged samples with 2.2 at. % O also revealed alignment of ω precipitates (Figure 2d). After ageing at 500 °C for 24 h, DA directly aged and OXA oxidized and aged microstructures showed larger sizes and decreased number densities of ω precipitates (Figure 3a-b), and the morphology differences with oxygen were more pronounced than at 450 °C. Specific grains close to the (100)₈ out of plane orientation after EBSD characterization were selected to characterize ω precipitate alignment with elevated oxygen levels. SEM-BSE and bright-field TEM images confirmed that ω particles were aligned along $<001>_{\beta}$ directions (Figure 3a-c). In addition, ω precipitates in the OXA—oxidized and aged samples exhibited cuboidal-like shapes faceted along the <001>₆ directions (**Figure 3c**) and also showed an elongated major axis aligned with $<111>_{\beta}$ directions that is typical for ω in Ti-Mo without O [5]. Finally, some regions with the highest oxygen levels of 2.2 at. % O in the OXA-oxidized and aged specimen aged at 500 °C showed the onset of lathlike α phase formation in addition to ω precipitates (**Figure 3d**), and this faster α precipitation rate during isothermal ageing is due to the stabilization of α with higher oxygen contents [13]. α precipitation was not observed for other oxygen levels in the DA directly aged and OXA oxidized and aged specimens aged at 500 °C for 24 h.

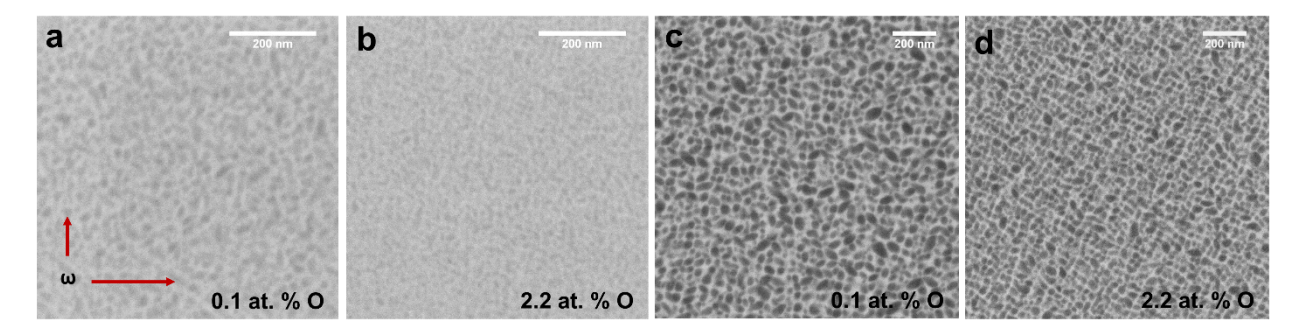


Figure 2. SEM-BSE images of DA directly aged and OXA oxidized and aged Ti-15Mo after ageing at 450 °C for (a-b) 2 h and (c-d) 24 h. DA Directly aged Ti-15Mo are shown in (a) and (c). OXA Oxidized and aged Ti-15Mo are shown in (b) and (d).

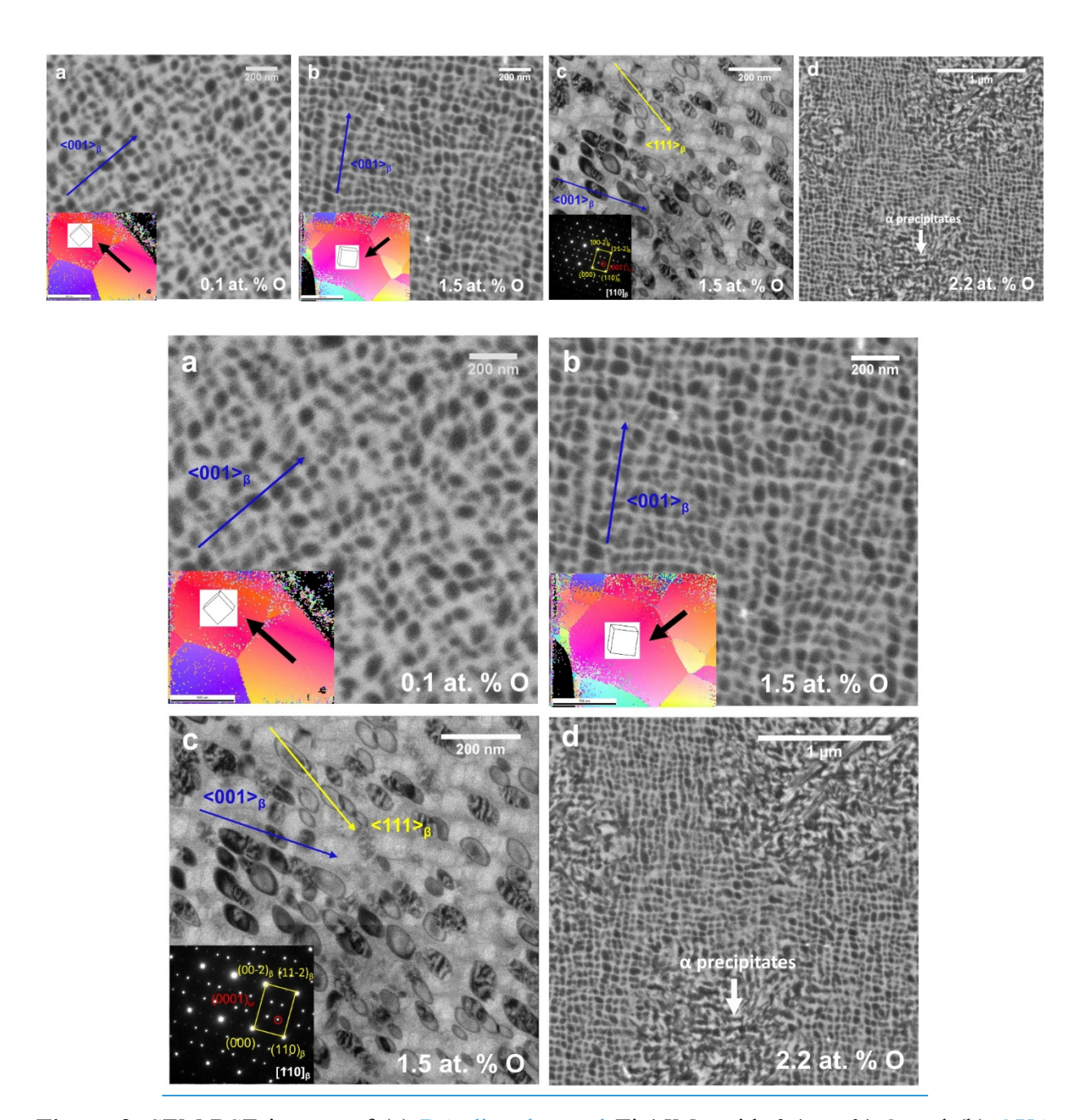


Figure 3. SEM-BSE images of (a) DA directly aged Ti-15Mo with 0.1 at. % O and (b) OXA oxidized and aged Ti-15Mo with 1.5 at. % O aged for 24 h at 500 °C. Insets show EBSD inverse pole figure maps with crystal grain orientations and the selected grain denoted by the black arrow with associated cubic lattice projection for microstructures in (a) and (b). (c) Bright-field TEM image of OXA-oxidized and aged Ti-15Mo aged for 24 h at 500 °C with 1.5 at. % O. Inset shows

SAED pattern for the $[110]_{\beta}$ zone axis showing β and ω diffraction spots. (d) SEM-BSE image of OXA-oxidized and aged Ti-15Mo with 2.2 at. % O aged for 24 h at 500 °C.

Size, aspect ratio, area density, and volume fraction of ω precipitates in DA-directly aged and OXA oxidized and aged specimens aged for 24 h at 450 °C and 500 °C were estimated using SEM-BSE images that showed all ω variants to compare differences in the aged microstructures (Table 1). The average lengths of the major and minor axes for ω were used to calculate an equivalent spherical diameter, 2r. After both 450 °C and 500 °C ageing, the measured equivalent diameter decreased with higher oxygen. The measured aspect ratio of ω particles based on the major and minor axes increased slightly without oxygen present. The area densities of ω particles, n_s , were estimated by counting ω particles in SEM-BSE images and dividing the total particle count by the area of the image. The area fraction of ω was estimated using image thresholding and measurement of SEM-BSE images using ImageJ processing software to be approximately 41 ± 1.1% for both DA directly aged and OXA oxidized and aged specimens aged at 450 °C and 500 °C. These area fractions were assumed to equal the volume fraction, f, of ω based on stereology [49]. The inter-particle spacing D for ω particles was calculated by taking into account the effect of finite obstacle size for impenetrable particles and represents the measure of the free spacing between finite obstacles [50]. The average planar radius $\langle r_s \rangle$ was calculated using $\langle r_s \rangle = \pi \langle$ r > /4, which was used to calculate D according to the following equation [50]:

$$D = [(32/3\pi f)^{1/2} - 2] < r_s > (Equation 1).$$

Table 1. Quantification of microstructural features for ω precipitates in aged Ti-15Mo with varying oxygen content.

Specimen	Ageing Treatment	Oxygen Concentration (at. %)	Oxygen nConcentration (wt. %)	Equivalent Diameter, 2r (nm)		Area Density, n _s (um ⁻²)	Interparticle spacing, D (nm)
DADirectly Aged	24 h, 450 °C		0.1	46 <u>± 1.8</u>	2.4 ± 0.3	271	16
OXAOxidized and Aged	24 h, 450 °C	2.2	0.7	32 ± 3.7	2.0 ± 0.1	501	11
Oxidized and AgedOXA	24 h, 500 °C	0.1	0.1	75 <u>±4.8</u>	23 <u>±</u> 0.2	181	26

216

In order to understand the extent of elemental partitioning to ω and β , APT measurements were performed after ageing at 450 °C and 500 °C. Reconstructed APT datasets from the OXA oxidized and aged specimen aged for 24 h at 450 °C with 2.2 at. % O (Figure 4) and aged for 24 h at 500 °C with 1.5 at. % O (Figure 5) showed Ti-rich regions and Mo-rich regions corresponding to the ω and β phases, respectively. Proximity histograms (or proxigrams) that were generated using iso-concentrations surfaces of 90 at. % Ti for OXA-oxidized and aged specimens aged at 450 °C and 500 °C showed that Ti partitioned to the ω phase while Mo partitioned to the β matrix, as has been reported in literature [48,51]. After ageing at 450 °C, O partitioned slightly to the ω phase, with up to 4.3 at. % O in ω compared to ~2 at. % O present in the β matrix (Figure 4b). O partitioned more significantly to ω in OXA-oxidized and aged Ti-15Mo aged at 500 °C, and the ω phase with ~3.5 at. % O contained three times as much oxygen content as in the β matrix with 1 at. % O (Figure 5b). This O partitioning behavior to ω during ageing has also been reported in the Ti-Nb-O system [35,36]. According to calculated proxigrams, the compositions for ω and β in OXA-oxidized and aged Ti-15Mo aged for 24 h at 500 °C with 1.5 at. % O are: 96.1 at. % Ti, 0.4 at. % Mo, 3.5 at. % O for ω and 85 at. % Ti, 14 at. % Mo, 1.0 at. % O for β .

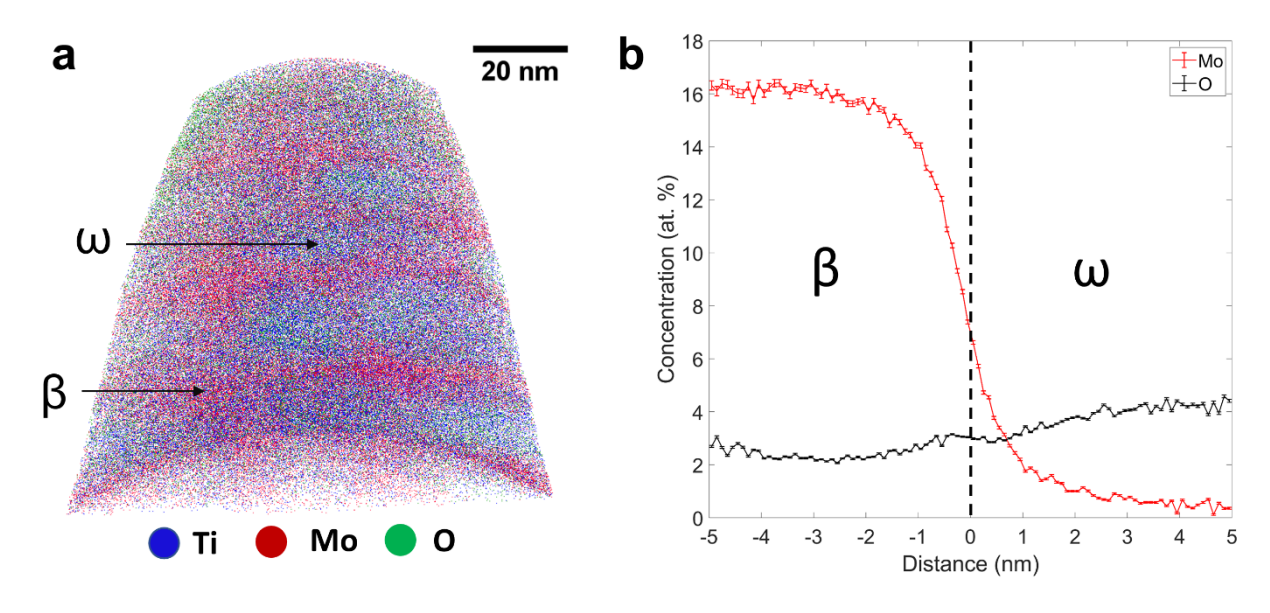


Figure 4. (a) APT reconstruction of OXA oxidized and aged Ti-15Mo aged for 24 h at 450 °C with 2.2 at. % O and (b) proxigram showing Mo and O concentration as a function of distance from 90 at. % Ti iso-concentration surfaces.

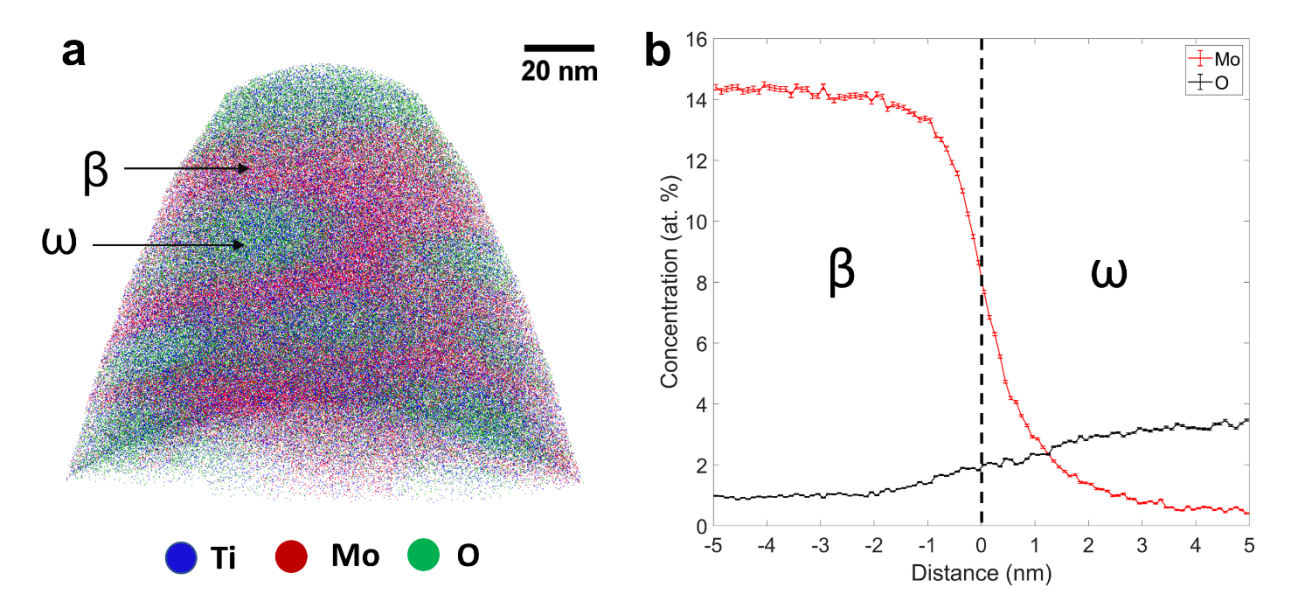


Figure 5. (a) APT reconstruction of OXA oxidized and aged Ti-15Mo aged for 24 h at 500 °C with 1.5 at. % O and (b) proxigram showing Mo and O concentration as a function of distance from 90 at. % Ti iso-concentration surfaces.

Micropillar compression was conducted to investigate the influence of elevated oxygen, ω precipitate size, and the corresponding microstructural changes on mechanical properties. Micropillars were fabricated for the DA-directly aged and OXA-oxidized and aged specimens aged at 450 and 500 °C for 24 hours. For the OXA-oxidized and aged specimen aged at 450 °C for 24 h, micropillars were fabricated at distances of ~100 μ m from the α lath / β matrix interface corresponding to 2.2 at. % O. Since the region corresponding to 2.2 at. % O in the OXA-oxidized and aged specimen aged at 500 °C for 24 h showed the onset of α precipitation in some regions (Figure 3d), micropillars were fabricated at a distance of ~300 μ m from the α lath / β matrix interface corresponding to 1.5 at. % O that showed only ω precipitation. Images of post-compression micropillars after 15% strain revealed differences in deformed morphologies with different oxygen contents (Figure 6). The deformed micropillars from the oxygen-free specimens showed prominent step-like features that corresponded to slip band formation during compression. Compressed pillars containing 2.2 and 1.5 at. % O also formed a large slip band after deformation,

although other finer slip traces were observed near the base of the pillar (located at blue arrow in Figure 6b, 6d).

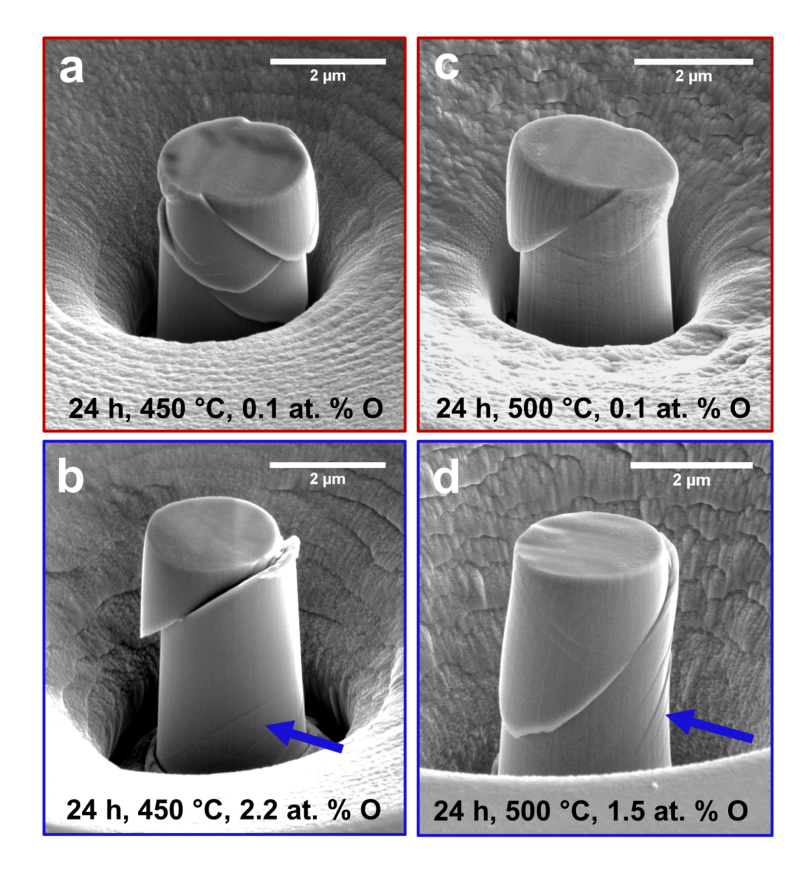


Figure 6. SEM-BSE images of 2 μm diameter micropillars compressed to 15% engineering strain for DA-directly aged and OXA-oxidized and aged Ti-15Mo after ageing for (a-b) 24 h at 450 °C, and (c-d) 24 h at 500 °C. DA-Directly aged Ti-15Mo are shown in (a) and (c). OXA-Oxidized and aged Ti-15Mo are shown in (b) and (d), with blue arrows showing fine slip traces.

The influence of oxygen on the compression response of the oxygen-containing micropillars differed for specimens aged at 450 °C and 500 °C (**Figure 7a-b**). Stress-strain curves for $\frac{DA-directly aged}{DA-directly aged}$ and $\frac{OXA-oxidized}{OXA-oxidized}$ and $\frac{Aged}{OXA-oxidized}$ specimens aged 450 °C both showed discontinuous and unstable flow during compression (**Figure 7a**). Significant drops in measured stress values for these curves corresponded to the observations of macroscale formation of slip bands (**Figure 6a-b**). The average yield strength and standard deviation values obtained from four tests per condition were 465 \pm 31 MPa and 457 \pm 27 MPa for specimens without oxygen and with 2.2 at. % O respectively. For $\frac{DA-directly aged}{DA-directly aged}$ and $\frac{OXA-oxidized}{DA-directly}$ aged at 500 °C and containing larger ω precipitates, stress-strain curves showed more stable plastic flow with

a slight drop or plateau in the engineering stress after initial yielding (**Figure 7b**). However, a significant increase in compressive yield strength is noted with elevated oxygen content and finer ω sizes. The average yield strength and standard deviation values were ~575 ± 37 MPa in the presence of oxygen, which significantly exceeded the average and standard deviation values of about 419 ± 31 MPa for DA-directly aged micropillars without oxygen. In order to understand the deformation mechanisms, TEM imaging was performed on liftout samples from cross-sections along [110] $_{\beta}$ for a compressed pillar with 1.5 at. % O (**Figure 7c**). Dark-field TEM images formed by selecting an ω reflection revealed that a continuous slip band cut through ω precipitates (blue arrow in **Figure 7c**). Slip trace analysis and direction of the slip bands observed in TEM images revealed that the bands were parallel to $[0001]_{\omega 1}$ // $[2-2-2]_{\beta}$ directions and perpendicular to the (1-12) $_{\beta}$ plane, indicating that dislocation activity took place along the <111>{112} $_{\beta}$ slip system. The formation of the continuous slip bands suggests that ω precipitates were sheared as a result of highly localized dislocation activity along the <111>{112} $_{\beta}$ system.

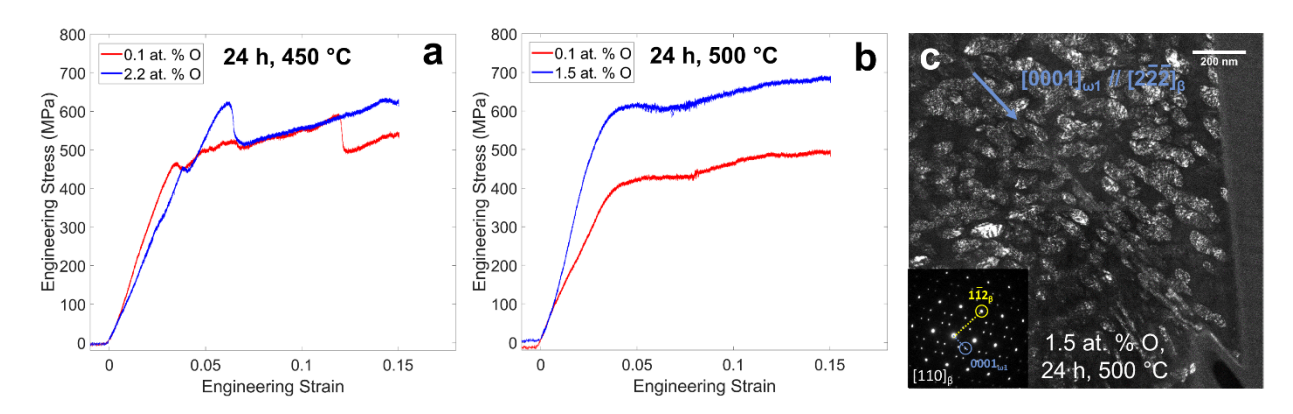


Figure 7. Engineering stress-strain curves for DA directly aged and OXA oxidized and aged Ti-15Mo after ageing for (a) 24 h at 450 °C and (b) 24 h at 500 °C. (c) Dark-field TEM image of liftout sample from compressed pillar to 15% strain for OXA oxidized and aged Ti-15Mo aged for 24 h at 500 °C with 1.5 at. % O showing sheared ω precipitates. Blue arrow points to sheared ω precipitates along $\langle 222 \rangle_{\beta}$ direction.

3.3. α precipitation and deformation in Ti-15Mo with varying oxygen content

Ageing treatments conducted at 600 °C yielded widespread α precipitation in DA-directly aged and OXA-oxidized and aged specimens, but the size and number density of α was directly influenced by oxygen content and sequence of heat treatment steps (**Figure 8**). Oxygen-free DA directly aged specimens aged for 4 h formed coarse α precipitates that were ~10 μ m in length (**Figure 8a**). In contrast, with 2.2 at. % O after the same heat treatment, a higher number density of finer α precipitates with approximately 0.5 to 2 μ m laths sizes was observed (**Figure 8b**). As a potent α -stabilizing element, oxygen is known to partition to the α phase during ageing of β Ti alloys [35], so very little oxygen is expected in the β matrix after α formation.

Two step ageing results (**Figure 8c-d**) showed additional α refinement for both DA-directly aged and OXA-oxidized and aged specimens compared to those aged directly in one step directly at 600 °C. The first step at 450 °C for 2 h allowed for ω precipitation (**Figure 2a-b**) that then acted as heterogeneous nucleation sites for α formation in the second 600 °C ageing step through ω -assisted α nucleation mechanisms [31,32,52]. The α microstructures observed after two step ageing also showed that elevated oxygen levels significantly increased the α number density. The combined effects of ω -assisted nucleation and oxygen-induced precipitation yielded the finest α precipitates of all observed conditions in OXA-oxidized and aged Ti-15Mo with two step ageing.

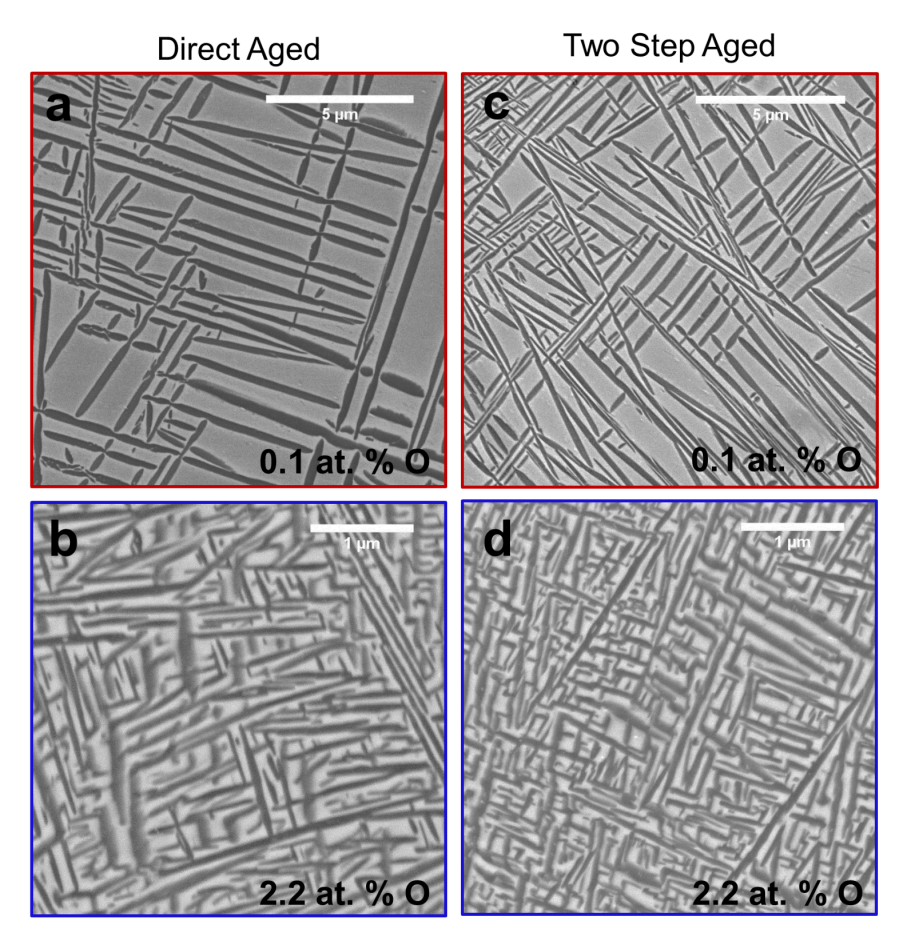


Figure 8. SEM-BSE images of (a) DA directly aged Ti-15Mo with 0.1 at. % O and (b) OXA oxidized and aged Ti-15Mo with 2.2 at. % O aged in one step for 4 h at 600 °C (Direct Aged), and (c) DA directly aged Ti-15Mo with 0.1 at. % O and (d) OXA oxidized and aged Ti-15Mo with 2.2 at. % O aged for 2 h at 450 °C, then for 4 h at 600 °C (Two Step Aged).

Micropillar compression testing of DA-directly aged and OXA-oxidized and aged specimens aged at 600 °C for 4 h was performed to understand changes in mechanical behavior with different α sizes and number densities. Oxygen-free compressed micropillars showed different morphologies depending on local α lath orientation in the pillar's volume. In some pillars, step formation and slip traces were observed near α/β interfaces (**Figure 9a**). Previously reported micropillar compression results for dual phase α - β Ti alloys also showed that slip may occur along the interface between α and β phases if oriented favorably relative to the deformation direction [53–55]. Alternatively, other micropillars did not show significant step formation and instead formed fine slip traces in the β matrix (**Figure 9b**). These variations in deformed pillar morphology

were attributed to the coarse α laths sizes observed after ageing that resulted in differences in α lath amounts and distributions in the tested micropillar volumes. In contrast, compressed pillars containing 2.2 at. % O (**Figure 9c-d**) showed a larger number of short slip traces that formed in multiple locations on pillar surfaces, suggesting more distributed deformation occurred than in the oxygen-free samples.

Compressive engineering stress-strain curves showed that the α lath size greatly influenced yield strength and curve shape (**Figure 9e**). Stress-strain curves for micropillars on DA-directly aged specimens directly aged in one step at 600 °C for 4 h showed significant scatter in compressive yield strengths ranging from 200-350 MPa. Additionally, little work hardening was observed after initial yielding for all DA micropillars, and the associated curves showed a plateau with a flat slope after yielding. In contrast, stress-strain curves from pillars with 2.2 at. % O after two step ageing displayed less variation in curve shapes and nearly doubled the compressive yield strengths (450-500 MPa), with improved work hardening after pillar yielding compared to directly aged specimens without O.

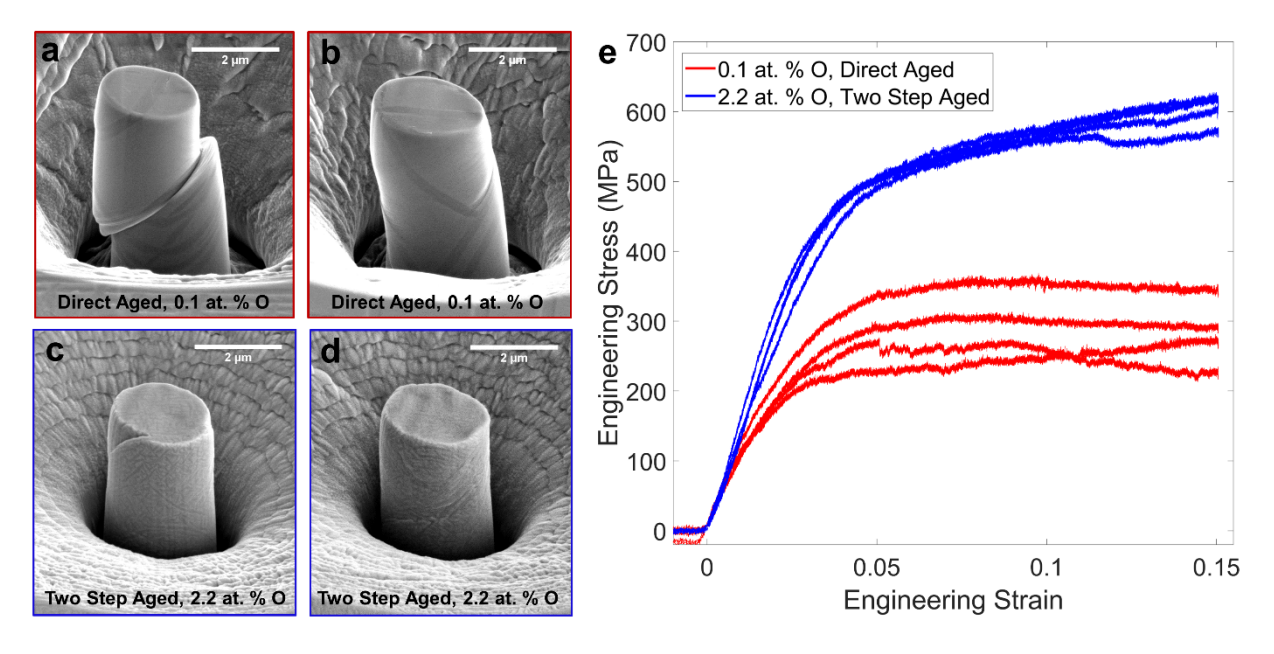


Figure 9. SEM-BSE images of 2 μm diameter micropillars compressed to 15% strain for (a-b) DA directly aged Ti-15Mo with 0.1 at. % O aged in one step for 4 h at 600 °C (Direct Aged) and (c-d) OXA oxidized and aged Ti-15Mo with 2.2 at. % O aged for 2 h at 450 °C, then 4 h at 600 °C (Two Step Aged). (e) Engineering stress-strain curves for DA directly aged Ti-15Mo with 0.1 at. % O aged in one step for 4 h at 600 °C (Direct Aged) and OXA oxidized and aged Ti-15Mo with 2.2 at. % O aged for 2 h at 450 °C, then 4 h at 600 °C (Two Step Aged).

4. Discussion

Aged microstructures and micropillar compression results revealed that interstitial oxygen levels obtained during oxidation directly influenced subsequent precipitate evolution and the associated mechanical properties of Ti-15Mo. In the single β phase matrix after oxidation, the maximum oxygen content was measured as 2.6 at. % O. Assuming equilibrium, this maximum oxygen level is controlled by the oxygen solubility limit in the β phase before inducing thermodynamic stabilization and precipitation of α . For Ti-Mo alloys, the extent of oxygen solubility in the metal substrate during oxidation has been reported to be influenced by the level of Mo, with higher Mo concentrations reducing the level of oxygen uptake by the substrate [56]. However, other metastable β Ti systems such as Ti-Nb based compositions have shown different maximum oxygen levels up to ~5 at. % obtained similarly through oxidation [36] or intentionally added to the bulk alloys [12,57,58]. The higher O solubility in the β phase for Ti-Nb compared to Ti-Mo alloys may be related to changes in the electron/atom (e/a) ratio [56], though the e/a ratios for Ti-15Mo and Ti-20Nb do not differ significantly with values of 4.24 and 4.2 respectively. However, pure Mo shows essentially no solubility for interstitial oxygen before forming oxide phases [59,60], while pure Nb allows for limited oxygen solubility prior to oxide formation [60]. In Nb-Mo alloys, oxygen solubility also decreases with increasing Mo content from ~2 at. % O in pure Nb to zero oxygen solubility with 75 at. % Mo [61]. Therefore, alloying Ti with Mo would likely reduce oxygen solubility compared to alloying Ti with Nb. The tailoring of oxygen solubility and maximum saturation levels via alloy chemistry design may allow for more pronounced effects regarding oxygen-induced phase transformations. Therefore, the maximum oxygen solubility in metastable β Ti alloys may be an important design consideration during development of future alloy compositions that intentionally utilize high oxygen levels.

Upon subsequent ageing at 450-500 °C, the microstructural evolution of ω precipitates in Ti-15Mo showed noticeable changes depending on oxygen content. Within Ti alloys, ω is known to form through a number of pathways including ellipsoidal nano-scale athermal ω through diffusionless transformation in compositions where the martensite start temperature is lower than the ω -start temperature and diffusional isothermal ω precipitation with ellipsoidal and/or cuboidal morphologies in more concentrated alloys upon ageing [5]. Plate-like or lamellar ω morphologies

have also been reported for ω formation under high pressure or shock loading [5] or during tensile deformation [62]. In the absence of oxygen and stress, ω -like embryos form in Ti-Mo by the partial displacive collapse of $\{111\}_{\beta}$ planes during rapid cooling after solution treatment [51]. With additional ageing, the full collapse of $\{111\}_{\beta}$ planes completes the β to ω transformation [51], and Mo is rejected from growing ω precipitates to the β matrix [5]. With elevated oxygen, oxygen partitions to ω precipitates (**Figure 5**) and several changes were noted including higher number densities and smaller ω precipitate sizes compared to specimens without oxygen (**Figure 2**, **Figure 3**). Such differences were also observed in the binary Ti-Nb system. In particular, the growth rate changes were attributed to possible kinetic barriers for the β to ω transformation with high oxygen [36]. More generally, ω precipitates grew more slowly in Ti-Mo compared to Ti-Nb for similar ageing treatments at all oxygen levels. This observation is consistent with prior studies showing slower ω nucleation and coarsening kinetics in oxygen-free Ti-Mo alloys compared to Ti-Nb systems [63]. This effect is attributed to the slower Mo diffusion rate compared to Nb in Ti [64] resulting in slower rejection of β -stabilizing elements during ω growth.

Oxygen also has a strong effect on ω precipitate morphology (Figure 3), with slightly faceted shapes and aligned particles seen with elevated oxygen compared to ellipsoidal shapes and more random arrangements without oxygen. The low lattice misfit Ti-Mo and Ti-Nb systems are known to yield ellipsoidal ω shapes, while higher misfit systems like Ti-V form cuboidal morphologies [5]. However, changes in ω's shape with elevated oxygen have been reported previously, such as for Ti-Nb that showed elongation along the major axis in the $<111>_{\beta}$ direction resulting in rod-like shapes [36]. The shape of ω in Ti-15Mo with high oxygen (Figure 3c) showed slight faceting along $<0.01>_{\beta}$ directions that matches the faceting of cuboidal ω observed in higher lattice misfit β Ti compositions such as the Ti-V system [65–67]. High oxygen levels may therefore result in the generation of additional misfit strains inducing the faceted ω morphologies in Ti-Mo. The alignment of ω precipitates with elevated oxygen (Figure 3b) was not observed in prior Ti-Nb studies [36]. Precipitate alignment has been widely reported for other metallic systems such as nickel [68–70] and cobalt superalloy [71,72] γ/γ microstructures driven by complex interactions between interfacial energy, misfit strains, and elastic stiffness. The aligned morphologies observed here for OXA-oxidized and aged Ti-15Mo suggest that the higher O levels may also result in possible changes for interfacial energy, misfit strains, and elastic stiffness that induce the observed aligned cuboidal-like microstructures.

The influence of oxygen on mechanical properties evaluated using micropillar compression was dependent on oxygen partitioning to ω precipitates and the size of ω precipitates after ageing. Although some oxygen partitioning was observed in OXA-oxidized and aged specimens aged for 24 h at 450 °C (Figure 4), little change was observed for compressive yield strength and work hardening behavior in DA directly aged and OXA oxidized and aged specimens (Figure 7a). With OXA-oxidized and aged Ti-15Mo aged for 24 h at 500 °C with 1.5 at. % O that contained larger oxygen-rich precipitates, micropillars showed higher compressive yield strength and marginal improvement in work hardening compared to specimens without oxygen (Figure 7b). Shearing and dissolution of isothermal coherent ω precipitates along the <111>{112} $_{\beta}$ slip system during deformation have been extensively reported in metastable β Ti alloys without oxygen [25,44,73– 76]. Observed in bulk tensile testing and micropillar compression, the precipitate shearing mechanism has been associated with embrittlement via the formation of precipitate-free channels, planar slip, localized slip band formation, and cavitation [25,44,74]. However, increased strength and improved work hardening behavior were reported for Ti-20Nb (at. %) containing oxygen that partitioned to larger ω precipitates [37]. Oxygen partitioning to ω increased ω's resistance to precipitate shearing and impeded precipitate shearing and the formation of continuous deformation channels, allowing for more homogeneous deformation to occur through dislocation bypassing [37]. To understand the role of oxygen in the Ti-Mo system and clarify ω-dislocation interactions, a similar analysis wais followed followed, and the stresses required for dislocations to shear or bypass ω particles were calculated for the Ti-15Mo microstructures observed here. The increase in critical resolved shear stress (CRSS) for ω precipitate shearing from modulus strengthening was estimated using the following equation [77]:

$$\Delta \tau_s = A(|\Delta G|)^{3/2} \left(\frac{fr}{Gb}\right)^{1/2}$$
 (Equation 2)

where A is a constant that was approximated as 0.013, ΔG the difference in shear modulus between ω precipitates and the β matrix, f the volume fraction of ω particles, 2r the equivalent diameter for ω , G the shear modulus of the β matrix, and b the Burgers vector of the β matrix. The increase in CRSS due to a dislocation bypassing mechanism through Orowan looping was also estimated for the investigated Ti-15Mo microstructures using the following equation [25,78]:

$$\Delta \tau_b = \frac{1}{1-\nu} \frac{Gb}{2\pi D} ln \frac{\sqrt{2/3}r}{b}$$
 (Equation 3)

where D is the inter-particle spacing. The values of Poisson's ratio ν and G of the β phase have been estimated for asimilar Ti-MoNb based gum metal alloys as 0.3619 [79] and 25-18 GPa [80]. respectively, using single crystal elastic constants measured with in-situ synchrotron x-ray diffraction [71,76]. The value of G for single-crystalline ω phase was estimated for pure Ti as 60 GPa [81]. Assuming the same values for Ti-15Mo and using the microstructural parameters given in **Table 1**, $\Delta \tau_s$ was calculated to exceed $\sim \frac{2500}{4000}$ MPa for all observed microstructures while $\Delta \tau_b$ ranged between $\sim 330-640230-440$ MPa, which reveals that the smaller applied stress for these two mechanisms is dislocation bypassing. Although the estimated values for $\Delta \tau_s$ and $\Delta \tau_b$ provide only relative comparisons for the stresses required to activate these mechanisms, this simple analysis suggests that dislocation bypassing is possible for the ω sizes observed here, as was also reported for Ti-20Nb microstructures in [37]. Even though dislocation bypassing is possible, the load drops and formation of slip bands in compressed micropillars for DA directly aged and OXA oxidized and aged Ti-15Mo aged for 24 h at 450 °C indicated that shearing of ω precipitates leading to continuous deformation channels still occurred. With oxygen partitioning to larger ω precipitates in OXA oxidized and aged Ti-15Mo aged for 24 h at 500 °C, compressive yield strength increased compared to DA directly aged specimens. However, the work hardening behavior did not improve significantly since ω precipitates were ultimately sheared (**Figure 7c**), unlike observations in Ti-20Nb with higher O levels where shearing of ω was suppressed [37]. This difference is attributed to the lower maximum O solubility in the β matrix of Ti-15Mo after oxidation compared to Ti-20Nb that resulted in a smaller amount of partitioned oxygen in ω. The lower oxygen level observed here may be less effective in strengthening ω precipitates against shearing. Similar results were observed with lower oxygen levels during micropillar testing with 1.5 at. % O in Ti-20Nb, which also showed slip band formation indicating shearing of ω during deformation [37]. These results suggest that work hardening and duetility improvements stemming from partitioned elevated oxygen in ω -containing β Ti alloys require a minimum amount of oxygen that is partly controlled by the maximum solubility of O. Oxygen solubility therefore becomes an important parameter in alloy design that employs this mechanism.

After ageing at 600 °C, elevated oxygen levels resulted in significant α precipitate refinement compared to specimens with minimal oxygen (**Figure 8**), observed both after direct ageing and with intentional prior ω formation in two step ageing. Rapid heating and direct ageing at 600 °C, which exceeds the reported 560 °C ω solvus [42], avoided potential β phase separation

and isothermal ω evolution known to promote heterogeneous α precipitation in β Ti alloys [82]. Also, athermal ω phase that has been reported for similar Ti-Mo compositions [51] and is likely present in solution treated and oxidized samples was expected to quickly dissolve upon rapid heating to 600 °C. In the absence of intermediate phases, the microstructural changes in α precipitate size and number density observed after direct ageing in a single step at 600 °C (Figure **8a-b**) are attributed to the increase in α nucleation driving force from elevated oxygen. Such differences have been demonstrated in a prior ageing study of the metastable β Ti-15-333 alloy with varying oxygen content [38]. Oxygen in solid solution is a potent α stabilizer in metastable β Ti alloys, and this stabilization increased the nucleation driving force for α leading to faster precipitation kinetics with a more refined lath size [38]. With two step ageing that intentionally formed ω prior to the 600 °C step (Figure 8c-d), ω-assisted nucleation, where ω acts as a heterogeneous nucleation agent for α [31–33], was combined with oxygen-induced α refinement to obtain the finest α lath sizes in OXA oxidized and aged specimens with 2.2 at. % O. During micropillar compression, significant variation was observed in the yield point of stress-strain curves for DA directly aged Ti-15Mo aged in one step directly at 600 °C (Figure 9e). This variation is attributed to intrinsic size effects related to the volume of tested micropillars relative to the α lath sizes. This type of size effect dominates when the micropillar's dimensions are on the order of microstructural features and the pillar's volume contains a small number density of dispersed obstacles, which leads to an observed size effect on measured yield strengths [83]. With smaller lath sizes in OXA oxidized and aged Ti-15Mo after two step ageing, this size effect was noticeably reduced, and the compressive yield strength roughly doubled compared to specimens without oxygen (Figure 9e). Many α precipitation refinement studies in metastable β Ti alloys have focused on obtaining finer α laths leading to increased tensile strengths after bulk testing [84] and compression strengths in micropillar investigations [54,55]. Since the α - β interface acts as the main barrier for dislocation motion in two phase Ti alloys, increased α number density results in a greater number of these interfaces to impede dislocation motion for higher strength in bulk testing [2,13]. Therefore, using elevated oxygen content to induce α lath refinement may offers an additional pathway to obtain high strength metastable β Ti alloys and can be combined with other mechanisms such as ω-assisted nucleation to yield even further refinement.

The results revealed the influence of oxygen in Ti-15Mo on ω and α precipitation and microstructural evolution that directly impacted compressive mechanical properties. While bulk

testing of the present alloys would be required to assess any change in ductility, other studies on oxygen containing β Ti alloys demonstrated strength increases without ductility reductions for annealed conditions [10,18]. The present findings illustrate beneficial effects of oxygen specifically for aged metastable β Ti alloys resulting in microstructural refinement and increased strength. The partitioning of oxygen to ω (Figure 5) and α precipitates [35] mitigates the known embrittlement challenges with interstitial O in β Ti [16], which opens possibilities for future alloy and processing development that intentionally utilizes oxygen as an alloying element in β Ti alloys. Furthermore, these findings may be used to understand the effects of higher oxygen levels in commercially relevant Ti-Mo based compositions, which could allow for increased oxygen concentration limits in industrial materials specifications. Overall, these results demonstrate that high oxygen levels induce phase transformation and precipitation changes during ageing that result in improved mechanical properties for Ti-15Mo.

5. Conclusions

The impact of high interstitial oxygen contents up to 2.6 at. % O, obtained using an oxidation exposure, on ω and α precipitation and the resulting effects on compressive mechanical properties were investigated for aged Ti-15Mo. The following conclusions were drawn:

- 1. High oxygen levels reduced the growth rate of ω precipitates and induced ω morphology changes from randomly arranged ellipsoidal shapes without O to cuboidal-like shapes aligned along $<001>_{\beta}$ directions with oxygen. O and Ti partitioning to ω and Mo partitioning to β were observed after ageing at both 450 and 500 °C. With the highest oxygen levels of 2.2 at. % O, α precipitation occurred in addition to ω formation after isothermal ageing at 500 °C.
- 2. The influence of oxygen on mechanical properties evaluated for ω-containing microstructures was dependent on oxygen partitioning to ω precipitates and ω precipitate size. Pillars with smaller oxygen-rich ω precipitates showed similar slip band formation, unstable plastic flow, and yield strength values as oxygen-free pillars. Pillars with larger oxygen-rich precipitates showed higher compressive yield strengths than oxygen-free pillars, but ω precipitate shearing, continuous deformation channels, and catastrophic slip were eventually observed. The strength improvement was attributed to hardening of the precipitates by oxygen.

- 3. After ageing at 600 °C, elevated oxygen levels induced finer α precipitate sizes with a higher number density compared to oxygen-free specimens. This refinement was due to an increased nucleation driving force for α precipitation with high oxygen contents resulting in faster nucleation of finer laths. Oxygen-induced refinement was also combined with the ω-assisted nucleation mechanism to obtain even smaller sizes for α precipitates.
- 4. The refined α precipitates obtained with elevated oxygen and two step ageing resulted in smaller size effects and higher compressive yield strengths during micropillar compression.

These results show the influence of high oxygen contents on ω and α precipitation with improvements to compressive mechanical properties in Ti-15Mo, which demonstrate the beneficial effects of intentional high oxygen levels in β Ti alloys and may be applicable to existing commercial alloy compositions as well as future alloy and processing design.

Acknowledgements

This work was supported by the National Science Foundation (NSF) through grant NSF CMMI-1729166 and the Graduate Research Fellowship Program under grant No. DGE 1256260. The authors would also like to thank Dr. John Foltz at ATI for providing the Ti-15Mo alloy material and Dr. Owen Neill at the Robert B. Mitchell Electron Microbeam Analysis Laboratory at the University of Michigan for assistance with WDS measurements and analysis.

References

- [1] R. Kolli, A. Devaraj, A Review of Metastable Beta Titanium Alloys, Metals (Basel). 8 (2018) 506. https://doi.org/10.3390/met8070506.
- [2] J.D. Cotton, R.D. Briggs, R.R. Boyer, S. Tamirisakandala, P. Russo, N. Shchetnikov, J.C. Fanning, State of the Art in Beta Titanium Alloys for Airframe Applications, Jom. 67 (2015) 1281–1303. https://doi.org/10.1007/s11837-015-1442-4.
- [3] M. Niinomi, M. Nakai, J. Hieda, Development of new metallic alloys for biomedical applications, Acta Biomater. 8 (2012) 3888–3903. https://doi.org/10.1016/j.actbio.2012.06.037.
- [4] A. Biesiekierski, J. Wang, M.A. Gepreel, C. Wen, A new look at biomedical Ti-based shape memory alloys, Acta Biomater. 8 (2012) 1661–1669. https://doi.org/10.1016/j.actbio.2012.01.018.

- [5] S. Banerjee, R. Tewari, G.K. Dey, Omega phase transformation morphologies and mechanisms, Int. J. Mater. Res. 97 (2006) 963–977. https://doi.org/10.3139/146.101327.
- [6] Y. Zheng, D. Banerjee, H.L. Fraser, A nano-scale instability in the β phase of dilute Ti–Mo alloys, Scr. Mater. 116 (2016) 131–134. https://doi.org/10.1016/j.scriptamat.2016.01.044.
- [7] H.L. Wang, Y.L. Hao, S.Y. He, T. Li, J.M. Cairney, Y.D. Wang, Y. Wang, E.G. Obbard, F. Prima, K. Du, S.J. Li, R. Yang, Elastically confined martensitic transformation at the nano-scale in a multifunctional titanium alloy, Acta Mater. 135 (2017) 330–339. https://doi.org/10.1016/j.actamat.2017.06.040.
- [8] Q. Liang, Y. Zheng, D. Wang, Y. Hao, R. Yang, Y. Wang, H.L. Fraser, Nano-scale structural non-uniformities in gum like Ti-24Nb-4Zr-8Sn metastable β-Ti alloy, Scr. Mater. 158 (2019) 95–99. https://doi.org/10.1016/j.scriptamat.2018.08.043.
- [9] Y. Zheng, S. Antonov, Q. Feng, R. Banerjee, D. Banerjee, H.L. Fraser, Shuffle-induced modulated structure and heating-induced ordering in the metastable β-titanium alloy, Ti-5Al-5Mo-5V-3Cr, Scr. Mater. 176 (2020) 7–11. https://doi.org/10.1016/j.scriptamat.2019.09.027.
- [10] T. Saito, T. Furuta, J.H. Hwang, S. Kuramoto, K. Nishino, N. Suzuki, R. Chen, A. Yamada, K. Ito, Y. Seno, T. Nonaka, H. Ikehata, N. Nagasako, C. Iwamoto, Y. Ikuhara, T. Sakuma, Multifunctional Alloys Obtained via a Dislocation-Free Plastic Deformation Mechanism, Science (80-.). 300 (2003) 464–467. https://doi.org/10.1126/science.1081957.
- [11] M. Besse, P. Castany, T. Gloriant, Mechanisms of deformation in gum metal TNTZ-O and TNTZ titanium alloys: A comparative study on the oxygen influence, Acta Mater. 59 (2011) 5982–5988. https://doi.org/10.1016/j.actamat.2011.06.006.
- [12] J. Il Kim, H.Y. Kim, H. Hosoda, S. Miyazaki, Shape Memory Behavior of Ti-22Nb-(0.5-2.0)O(at%) Biomedical Alloys, Mater. Trans. 46 (2005). https://doi.org/10.2320/matertrans.46.852.
- [13] D. Banerjee, J.C. Williams, Perspectives on Titanium Science and Technology, Acta Mater. 61 (2013) 844–879. https://doi.org/10.1016/j.actamat.2012.10.043.
- [14] P. Kofstad, High-Temperature Oxidation of Titanium, J. Less-Common Met. 12 (1967) 449–464. https://doi.org/Doi 10.1016/0022-5088(67)90017-3.
- [15] I. Gurrappa, A.K. Gogia, High performance coatings for titanium alloys to protect against oxidation, Surf. Coatings Technol. 139 (2001). https://doi.org/10.1016/S0257-8972(00)01137-3.
- [16] Z. Liu, G. Welsch, Effects of oxygen and heat treatment on the mechanical properties of alpha and beta titanium alloys, Metall. Trans. A. 19 (1988) 527–542. https://doi.org/10.1007/bf02649267.
- [17] H. Conrad, Effect of interstitial solutes on the strength and ductility of titanium, Prog. Mater. Sci. 26 (1981) 123–403. https://doi.org/10.1016/0079-6425(81)90001-3.

- [18] V. Jablokov, N. Murray, H. Rack, H. Freese, Influence of Oxygen Content on the Mechanical Properties of Titanium-35Niobium-7Zirconium-5Tantalum Beta Titanium Alloy, J. ASTM Int. 2 (2005) 12776. https://doi.org/10.1520/JAI12776.
- [19] M. Tahara, H.Y. Kim, T. Inamura, H. Hosoda, S. Miyazaki, Lattice modulation and superelasticity in oxygen-added β-Ti alloys, Acta Mater. 59 (2011) 6208–6218. https://doi.org/10.1016/j.actamat.2011.06.015.
- [20] T. Li, M. Lai, A. Kostka, S. Salomon, S. Zhang, C. Somsen, M.S. Dargusch, D. Kent, Composition of the nanosized orthorhombic O' phase and its direct transformation to fine α during ageing in metastable β-Ti alloys, Scr. Mater. 170 (2019) 183–188. https://doi.org/10.1016/j.scriptamat.2019.06.008.
- [21] A. Ramarolahy, P. Castany, F. Prima, P. Laheurte, I. Peron, T. Gloriant, Microstructure and mechanical behavior of superelastic Ti-24Nb-0.5O and Ti-24Nb-0.5N biomedical alloys, J Mech Behav Biomed Mater. 9 (2012) 83–90. https://doi.org/10.1016/j.jmbbm.2012.01.017.
- [22] L.S. Wei, H.Y. Kim, T. Koyano, S. Miyazaki, Effects of oxygen concentration and temperature on deformation behavior of Ti-Nb-Zr-Ta-O alloys, Scr. Mater. 123 (2016) 55–58. https://doi.org/10.1016/j.scriptamat.2016.05.043.
- [23] L.S. Wei, H.Y. Kim, S. Miyazaki, Effects of oxygen concentration and phase stability on nano-domain structure and thermal expansion behavior of Ti–Nb–Zr–Ta–O alloys, Acta Mater. 100 (2015) 313–322. https://doi.org/10.1016/j.actamat.2015.08.054.
- [24] J.C. Williams Hickman, B.S., Marcus, H.L., The effect of omega phase on the mechanical properties of titanium alloys, Metall. Trans. 2 (1971) 1913–1919. https://doi.org/10.1007/BF02913423.
- [25] A. Gysler, G. Lütjering, V. Gerold, Deformation behavior of age-hardened Ti-Mo alloys, Acta Metall. 22 (1974) 901–909. https://doi.org/10.1016/0001-6160(74)90057-1.
- [26] M.J. Lai, T. Li, F.K. Yan, J.S. Li, D. Raabe, Revisiting ω phase embrittlement in metastable β titanium alloys: Role of elemental partitioning, Scr. Mater. 193 (2021) 38– 42. https://doi.org/10.1016/j.scriptamat.2020.10.031.
- [27] M.J. Lai, T. Li, D. Raabe, ω phase acts as a switch between dislocation channeling and joint twinning- and transformation-induced plasticity in a metastable β titanium alloy, Acta Mater. 151 (2018) 67–77. https://doi.org/10.1016/j.actamat.2018.03.053.
- [28] B. Ellyson, J. Klemm-Toole, K. Clarke, R. Field, M. Kaufman, A. Clarke, Tuning the strength and ductility balance of a TRIP titanium alloy, Scr. Mater. 194 (2021) 113641. https://doi.org/10.1016/j.scriptamat.2020.113641.
- [29] J. Gao, A.J. Knowles, D. Guan, W.M. Rainforth, ω phase strengthened 1.2GPa metastable β titanium alloy with high ductility, Scr. Mater. 162 (2019) 77–81. https://doi.org/10.1016/j.scriptamat.2018.10.043.
- [30] F. Sun, J.Y. Zhang, P. Vermaut, D. Choudhuri, T. Alam, S.A. Mantri, P. Svec, T. Gloriant, P.J. Jacques, R. Banerjee, F. Prima, Strengthening strategy for a ductile metastable β-titanium alloy using low-temperature aging, Mater. Res. Lett. 5 (2017) 547–

- 553. https://doi.org/10.1080/21663831.2017.1350211.
- [31] F. Prima, P. Vermaut, G. Texier, D. Ansel, T. Gloriant, Evidence of α-nanophase heterogeneous nucleation from ω particles in a β-metastable Ti-based alloy by high-resolution electron microscopy, Scr. Mater. 54 (2006). https://doi.org/10.1016/j.scriptamat.2005.10.024.
- [32] Y. Zheng, R.E.A. Williams, D. Wang, R. Shi, S. Nag, P. Kami, J.M. Sosa, R. Banerjee, Y. Wang, H.L. Fraser, Role of ω phase in the formation of extremely refined intragranular α precipitates in metastable β-titanium alloys, Acta Mater. 103 (2016) 850–858. https://doi.org/10.1016/j.actamat.2015.11.020.
- [33] T. Li, D. Kent, G. Sha, H. Liu, S.G. Fries, A. V Ceguerra, M.S. Dargusch, J.M. Cairney, Nucleation driving force for ω-assisted formation of α and associated ω morphology in β-Ti alloys, Scr. Mater. 155 (2018) 149–154. https://doi.org/10.1016/j.scriptamat.2018.06.039.
- [34] R. Shi, Y. Zheng, R. Banerjee, H.L. Fraser, Y. Wang, ω-Assisted α nucleation in a metastable β titanium alloy, Scr. Mater. 171 (2019) 62–66. https://doi.org/10.1016/j.scriptamat.2019.06.020.
- [35] M. Niinomi, M. Nakai, M. Hendrickson, P. Nandwana, T. Alam, D. Choudhuri, R. Banerjee, Influence of oxygen on omega phase stability in the Ti-29Nb-13Ta-4.6Zr alloy, Scr. Mater. 123 (2016) 144–148. https://doi.org/10.1016/j.scriptamat.2016.06.027.
- [36] K. Chou, E.A. Marquis, Oxygen effects on ω and α phase transformations in a metastable β Ti–Nb alloy, Acta Mater. 181 (2019) 367–376. https://doi.org/10.1016/j.actamat.2019.09.049.
- [37] K. Chou, N. Li, E.A. Marquis, Enhanced work hardening from oxygen-stabilized ω precipitates in an aged metastable β Ti-Nb alloy, <u>Acta Materialia</u>. <u>Submitted In review</u>. (2021).
- [38] K. Chou, O. Neill, E.A. Marquis, Oxygen-induced refinement of α precipitates in an aged metastable β Ti-15-333 alloy, Scripta Materialia. Submitted Accepted. (2021).
- [39] X. Ji, S. Emura, T. Liu, K. Suzuta, X. Min, K. Tsuchiya, Effect of oxygen addition on microstructures and mechanical properties of Ti-7.5Mo alloy, J. Alloys Compd. 737 (2018) 221–229. https://doi.org/10.1016/j.jallcom.2017.12.072.
- [40] X. Min, P. Bai, S. Emura, X. Ji, C. Cheng, B. Jiang, K. Tsuchiya, Effect of oxygen content on deformation mode and corrosion behavior in β-type Ti-Mo alloy, Mater. Sci. Eng. A. 684 (2017) 534–541. https://doi.org/10.1016/j.msea.2016.12.062.
- [41] Y. Zheng, T. Alam, R. Banerjee, D. Banerjee, H.L. Fraser, The influence of aluminum and oxygen additions on intrinsic structural instabilities in titanium-molybdenum alloys, Scr. Mater. 152 (2018) 150–153. https://doi.org/10.1016/j.scriptamat.2018.04.030.
- [42] P. Zháňal, P. Harcuba, M. Hájek, B. Smola, J. Stráský, J. Šmilauerová, J. Veselý, M. Janeček, Evolution of ω phase during heating of metastable β titanium alloy Ti–15Mo, J. Mater. Sci. 53 (2018) 837–845. https://doi.org/10.1007/s10853-017-1519-2.

- [43] H. Zhang, B.E. Schuster, Q. Wei, K.T. Ramesh, The design of accurate microcompression experiments, Scr. Mater. 54 (2006) 181–186. https://doi.org/10.1016/j.scriptamat.2005.06.043.
- [44] W. Chen, J. Zhang, S. Cao, Y. Pan, M. Huang, Q. Hu, Q. Sun, L. Xiao, J. Sun, Strong deformation anisotropies of ω -precipitates and strengthening mechanisms in Ti-10V-2Fe-3Al alloy micropillars: Precipitates shearing vs precipitates disordering, Acta Mater. 117 (2016) 68–80. https://doi.org/10.1016/j.actamat.2016.06.065.
- [45] C. Shin, H. h Jin, H. Sung, D.J. Kim, Y.S. Choi, K. Oh, Evaluation of Irradiation Effects on Fracture Strength of Silicon Carbide using Micropillar Compression Tests, Exp. Mech. 53 (2012) 687–697. https://doi.org/10.1007/s11340-012-9678-1.
- [46] P. Samimi, Y. Liu, I. Ghamarian, P.C. Collins, A novel tool to assess the influence of alloy composition on the oxidation behavior and concurrent oxygen-induced phase transformations for binary Ti–xMo alloys at 650°C, Corros. Sci. 89 (2014). https://doi.org/10.1016/j.corsci.2014.09.010.
- [47] Z. Liu, G. Welsch, Literature Survey on Diffusivities of Oxygen, Aluminum, and Vanadium in Alpha Titanium, Beta Titanium, and in Rutile, Metall. Trans. A. 19 (1988) 1121–1125. https://doi.org/10.1007/BF02628396.
- [48] A. Devaraj, R.E.A. Williams, S. Nag, R. Srinivasan, H.L. Fraser, R. Banerjee, Three-dimensional morphology and composition of omega precipitates in a binary titanium—molybdenum alloy, Scr. Mater. 61 (2009). https://doi.org/10.1016/j.scriptamat.2009.06.006.
- [49] G. Vander Voort, Measurement of Microstructure, in: Met. Handb. Desk Ed., ASM International, 1998. https://doi.org/10.31399/asm.hb.mhde2.a0003248.
- [50] A.J. Ardell, Precipitation hardening, Metall. Trans. A. 16 (1985) 2131–2165. https://doi.org/10.1007/BF02670416.
- [51] A. Devaraj, S. Nag, R. Srinivasan, R.E.A. Williams, S. Banerjee, R. Banerjee, H.L. Fraser, Experimental evidence of concurrent compositional and structural instabilities leading to ω precipitation in titanium–molybdenum alloys, Acta Mater. 60 (2012) 596–609. https://doi.org/10.1016/j.actamat.2011.10.008.
- [52] T. Li, D. Kent, G. Sha, L.T. Stephenson, A. V Ceguerra, S.P. Ringer, M.S. Dargusch, J.M. Cairney, New insights into the phase transformations to isothermal ω and ω-assisted α in near β-Ti alloys, Acta Mater. 106 (2016) 353–366. https://doi.org/10.1016/j.actamat.2015.12.046.
- [53] T.-S. Jun, G. Sernicola, F.P.E. Dunne, T.B. Britton, Local deformation mechanisms of two-phase Ti alloy, Mater. Sci. Eng. A. 649 (2016). https://doi.org/10.1016/j.msea.2015.09.016.
- [54] W. Kou, Q. Sun, L. Xiao, J. Sun, Coupling effect of second phase and phase interface on deformation behaviours in microscale Ti-55531 pillars, J. Alloys Compd. 820 (2020) 153421. https://doi.org/10.1016/j.jallcom.2019.153421.
- [55] W. Kou, Q. Sun, L. Xiao, J. Sun, Superior plasticity stability and excellent strength in Ti-

- 55531 alloy micropillars via harmony slip in nanoscale α/β phases, Sci. Rep. 9 (2019). https://doi.org/10.1038/s41598-019-41574-7.
- [56] P. Samimi, D.A. Brice, I. Ghamarian, Y. Liu, P.C. Collins, Systematic Assessment of the Influence of Mo Concentration on the Oxygen Ingress in Ti–Mo System During High Temperature Oxidation, Oxid. Met. 85 (2016). https://doi.org/10.1007/s11085-015-9600-1.
- [57] Q. Wei, L. Wang, Y. Fu, J. Qin, W. Lu, D. Zhang, Influence of oxygen content on microstructure and mechanical properties of Ti–Nb–Ta–Zr alloy, Mater. Des. 32 (2011). https://doi.org/10.1016/j.matdes.2010.11.049.
- [58] B. Yuan, B. Yang, Y. Gao, M. Lai, X.H. Chen, M. Zhu, Achieving ultra-high superelasticity and cyclic stability of biomedical Ti–11Nb–4O (at.%) alloys by controlling Nb and oxygen content, Mater. Des. 92 (2016). https://doi.org/10.1016/j.matdes.2015.12.148.
- [59] L. Brewer, R.H. Lamoreaux, The Mo-O system (Molybdenum-Oxygen), Bull. Alloy Phase Diagrams. 1 (1980) 85–89. https://doi.org/10.1007/BF02881199.
- [60] J.J. English, D.M.I.C. (U.S.), Binary and ternary phase diagrams of columbium, molybdenum, tantalum, and tungsten, (1961) 1 volume (various pagings). file://catalog.hathitrust.org/Record/102326559.
- [61] R.. Bryant, The solubility of oxygen in transition metal alloys, J. Less Common Met. 4 (1962). https://doi.org/10.1016/0022-5088(62)90060-7.
- [62] H. Liu, M. Niinomi, M. Nakai, K. Cho, H. Fujii, Deformation-induced ω-phase transformation in a β-type titanium alloy during tensile deformation, Scr. Mater. 130 (2017) 27–31. https://doi.org/10.1016/j.scriptamat.2016.10.036.
- [63] J. Coakley, B.-S. Seong, D. Dye, M. Ohnuma, Isothermal omega kinetics in beta-titanium alloys, Philos. Mag. Lett. 97 (2017). https://doi.org/10.1080/09500839.2017.1282633.
- [64] G.B. Gibbs, D. Graham, D.H. Tomlin, Diffusion in titanium and titanium—niobium alloys, Philos. Mag. 8 (1963). https://doi.org/10.1080/14786436308207292.
- [65] J.C. Williams, M.J. Blackburn, The Influence of Misfit on the Morphology and Stability of the Omega Phase in Titanium-Transition Metal Alloys, Trans. Metall. Soc. AIME. 245 (1969) 2352–2355.
- [66] B.S. Hickman, The formation of omega phase in titanium and zirconium alloys: A review, J. Mater. Sci. 4 (1969) 554–563. https://doi.org/10.1007/bf00550217.
- [67] D. Choudhuri, Y. Zheng, T. Alam, R. Shi, M. Hendrickson, S. Banerjee, Y. Wang, S.G. Srinivasan, H. Fraser, R. Banerjee, Coupled experimental and computational investigation of omega phase evolution in a high misfit titanium-vanadium alloy, Acta Mater. 130 (2017) 215–228. https://doi.org/10.1016/j.actamat.2017.03.047.
- [68] J.K. Tien, S.M. Copley, The effect of orientation and sense of applied uniaxial stress on the morphology of coherent gamma prime precipitates in stress annealed nickel-base superalloy crystals, Metall. Trans. 2 (1971). https://doi.org/10.1007/BF02663347.

- [69] J.K. Tien, S.M. Copley, The effect of uniaxial stress on the periodic morphology of coherent gamma prime precipitates in nickel-base superalloy crystals, Metall. Trans. 2 (1971). https://doi.org/10.1007/BF02662660.
- [70] M. Kamaraj, Rafting in single crystal nickel-base superalloys An overview, Sadhana. 28 (2003). https://doi.org/10.1007/BF02717129.
- [71] A. Suzuki, H. Inui, T.M. Pollock, L1 ₂ -Strengthened Cobalt-Base Superalloys, Annu. Rev. Mater. Res. 45 (2015). https://doi.org/10.1146/annurev-matsci-070214-021043.
- [72] A.M. Jokisaari, S.S. Naghavi, C. Wolverton, P.W. Voorhees, O.G. Heinonen, Predicting the morphologies of γ' precipitates in cobalt-based superalloys, Acta Mater. 141 (2017). https://doi.org/10.1016/j.actamat.2017.09.003.
- [73] A.W. Bowen, Omega phase embrittlement in aged Ti-15%Mo, Scr. Metall. 5 (1971). https://doi.org/10.1016/0036-9748(71)90258-4.
- [74] M.J. Lai, C.C. Tasan, D. Raabe, Deformation mechanism of ω-enriched Ti–Nb-based gum metal: Dislocation channeling and deformation induced ω–β transformation, Acta Mater. 100 (2015) 290–300. https://doi.org/10.1016/j.actamat.2015.08.047.
- [75] S.A. Mantri, D. Choudhuri, T. Alam, V. Ageh, F. Sun, F. Prima, R. Banerjee, Change in the deformation mode resulting from beta-omega compositional partitioning in a Ti Mo alloy: Room versus elevated temperature, Scr. Mater. 130 (2017) 69–73. https://doi.org/10.1016/j.scriptamat.2016.11.013.
- [76] T.W. Duerig, G.T. Terlinde, J.C. Williams, Phase transformations and tensile properties of Ti-10V-2Fe-3AI, Metall. Trans. A. 11 (1980) 1987–1998. https://doi.org/10.1007/bf02655118.
- [77] E. Nembach, Particle Strengthening of Metals and Alloys, Wiley, New York, 1997.
- [78] M.F. Ashby, Oxide Dispersion Strengthening, in: G.S. Ansell, T.D. Cooper, F.V. Lenel (Eds.), Gordon & Breach, 1968.
- [79] K. Václavová, J. Stráský, V. Polyakova, J. Stráská, J. Nejezchlebová, H. Seiner, I. Semenova, M. Janeček, Microhardness and microstructure evolution of ultra-fine grained Ti-15Mo and TIMETAL LCB alloys prepared by high pressure torsion, Mater. Sci. Eng. A. 682 (2017) 220–228. https://doi.org/10.1016/j.msea.2016.11.038.
- [80] R. Sahara, S. Emura, S. Ii, S. Ueda, K. Tsuchiya, First-principles study of electronic structures and stability of body-centered cubic Ti–Mo alloys by special quasirandom structures, Sci. Technol. Adv. Mater. 15 (2014) 035014. https://doi.org/10.1088/1468-6996/15/3/035014.
- [81] M. Tane, Y. Okuda, Y. Todaka, H. Ogi, A. Nagakubo, Elastic properties of single-crystalline ω phase in titanium, Acta Mater. 61 (2013) 7543–7554. https://doi.org/10.1016/j.actamat.2013.08.036.
- [82] O.M. Ivasishin, P.E. Markovsky, Y.V. Matviychuk, S.L. Semiatin, C.H. Ward, S. Fox, A comparative study of the mechanical properties of high-strength β-titanium alloys, J. Alloys Compd. 457 (2008). https://doi.org/10.1016/j.jallcom.2007.03.070.

- [83] J.P. Wharry, K.H. Yano, P. V Patki, Intrinsic-extrinsic size effect relationship for micromechanical tests, Scr. Mater. 162 (2019) 63–67. https://doi.org/10.1016/j.scriptamat.2018.10.045.
- [84] S.A. Mantri, D. Choudhuri, T. Alam, G.B. Viswanathan, J.M. Sosa, H.L. Fraser, R. Banerjee, Tuning the scale of α precipitates in β-titanium alloys for achieving high strength, Scr. Mater. 154 (2018) 139–144. https://doi.org/10.1016/j.scriptamat.2018.05.040.